Fast physical reservoir computing, achieved with nonlinear interfered spin waves

NEUROMORPHIC
Computing and Engineering

PAPER

Fast physical reservoir computing, achieved with nonlinear interfered spin waves

Wataru Namiki[1], **Daiki Nishioka**[1,2], **Takashi Tsuchiya**[1,*] and **Kazuya Terabe**[1]

[1] Research Center for Materials Nanoarchitectonics, National Institute for Materials Science, Ibaraki, Japan
[2] Department of Applied Physics, Tokyo University of Science, Tokyo, Japan
* Author to whom any correspondence should be addressed.

E-mail: TSUCHIYA.Takashi@nims.go.jp

Keywords: Reservoir computing, spin wave interference, artificial intelligence

Supplementary material for this article is available online

OPEN ACCESS

RECEIVED
29 December 2023

REVISED
18 April 2024

ACCEPTED FOR PUBLICATION
10 June 2024

PUBLISHED
20 June 2024

Abstract

Reservoir computing is a promising approach to implementing high-performance artificial intelligence that can process input data at lower computational costs than conventional artificial neural networks. Although reservoir computing enables real-time processing of input time-series data on artificial intelligence mounted on terminal devices, few physical devices are capable of high-speed operation for real-time processing. In this study, we introduce spin wave interference with a stepped input method to reduce the operating time of the physical reservoir, and second-order nonlinear equation task and second-order nonlinear autoregressive mean averaging, which are well-known benchmark tasks, were carried out to evaluate the operating speed and prediction accuracy of said physical reservoir. The demonstrated reservoir device operates at the shortest operating time of 13 ms/5000-time steps, compared to other compact reservoir devices, even though its performance is higher than or comparable to such physical reservoirs. This study is a stepping stone toward realizing an artificial intelligence device capable of real-time processing on terminal devices.

1. Introduction

Reservoir computing is a promising approach to implementing high-performance artificial intelligence that can process input data at lower computational costs than conventional artificial neural networks since the reservoir computing system trains only output weights as parameters and exhibits the sufficient ability to process time-series data [1–4]. This feature of reservoir computing arises from three key features: nonlinear response, short-term memory, and the ability to map input information in higher dimensional feature space. Said reservoir computing enables real-time processing of input information, such as time-series data on artificial intelligence mounted on the terminal device, namely 'edge-computing.' To implement such edge computing, it is needed physical reservoir computing that operates on a terminal device with limited electric power can be carried out with a physical device satisfying the three features mentioned above. In recent years, various physical systems, such as electrical circuits, electrochemical cells, magnetics, optical elements, robotics, ion-gating devices, and so on, have been utilized to build reservoir computing systems based on physical dynamics [4–49]. However, some issues still need to be addressed due to the slow operation speed, high electrical power consumption, insufficient accuracy rate, and enormous volumes associated with such systems. In particular, slow operation speed is a fatal issue when realizing real-time processing. While the optical circuit shows the fastest operation speed of approximately 2 ms among physical reservoirs, the circuit size is enormous due to the long feedback loop of 280 meters [26]. Thus, it is challenging to integrate such circuits on a terminal device consisting of compact elements. The spin wave, a collective excitation motion of wave-shaped magnetization with phase, is attracting attention among related research fields due to its advantage of a charge-less transport method, which reduces electric power consumption [50–53]. In recent years, reservoir computing systems with spin wave propagation in an active-ring resonator have been

proposed. However, its capabilities could be better due to the large volume resulting from the circuit structure and its computational performance [17–19]. To overcome such problems, it has been shown that the physical device with spin wave interference, proposed by micromagnetic simulation [40–45], satisfies the following features of the physical reservoir by an experimental demonstration in our previous study [46]. Although the experimental demonstration revealed relatively fast operation comparable to the optical circuit using optical dynamics [46], no experimental demonstration has explored realizing the fastest processing speed thus far.

Herein, we improve the operation speed of compact physical reservoirs utilizing spin wave interference to realize real-time processing of physical reservoir computing. A spin wave is excited by resonance with magnetic field switching induced by an electrical signal's rising or falling edge [54]. In this study, the conversion method for input data is changed from pulsed voltage input used in the previous study to stepped voltage input. This change can reduce the length of input time-series voltage dominating the operating time of the physical device since the rising or falling edge of the pulsed signal, which consists of a rising edge and a falling edge, is no longer necessary. This is because a stepped signal has only a falling edge or rising edge, while a pulsed signal has falling and rising edges. This method can reduce operating time by up to 11.8% while maintaining high performance superior to other physical reservoirs.

2. Experimental methods

2.1. Fabrication of the physical device for reservoir computing with interfered spin wave multi-detection

The physical device is the same one used in the previous study [46]. A $Y_3Fe_5O_{12}$ single crystal with a diameter and thickness of 5.0 and 0.5 mm, respectively, was used in this study, and its surface is 111 plane. Coplanar waveguides (CPWs) were fabricated using 90 nm-thick Au thin films on ten nm-thick Ti adherent layers. A signal line (S) and two ground lines (G) of a CPW are 10 μm wide and 20 μm wide, respectively. The edges of adjacent CPWs are separated by 30 μm [46].

2.2. Measurement setup of the physical device

All experimental measurement was performed at a room temperature of 295 $\pm$ 1 K. A magnetic field H was applied to the 111 direction. The exciters and detectors shown in figure 1(a) were connected to an arbitrary waveform generator and an oscilloscope through GSG probes, respectively. Stepped voltage with transient times (i.e. rise time or fall time) of 280 ps was input to the exciter antenna for spin wave excitation. The amplitude of the stepped voltage was set to 280 mV. Then, the input and detected signals were amplified through amplifiers. Five hundred times accumulation was carried out to reduce the noise component in the detected signal. On a nonlinear time-series data processing task, a random waveform was transformed into a stepped voltage waveform with various durations ranging from 2 to 20 ns. The converted waveform has a discrete time step k of 5000. To remove the history of the last waveform, an interval of 4 μs was inserted after the input waveform signal.

This study used two exciters (Exciter A and Exciter B) and two detectors (Detector A and Detector B). To measure spin wave, (1) In the case of 'with interference' and 'with multi-detection', both exciters and both detectors were used simultaneously. (2) In the case of 'with interference' and 'without multi-detection', both exciters and one detector (i.e., Detector A) were used. (3) In the case of 'without interference' and 'without multi-detection', one exciter (i.e. only Exciter A) and one of the detectors (i.e. Detector A or Detector B) were used. The previous work also shows the details of the measurement setup [46].

H ranges from 100–400 mT at a 10 mT step to evaluate the spin wave property and from 150–250 mT to evaluate the processing performance of the physical reservoir.

2.3. Evaluation of spin wave property

The wave number k_w of the electric current density $j(x)$ reflects that of a spin wave excited by an oersted field induced by the $j(x)$ flowing in the CPW. The $j(x)$ in a CPW is written as follows [55];

$$j(x) = \begin{cases} -1 & -\left(\frac{l_S}{2}+l_1+l_G\right) \leqslant x \leqslant -\left(\frac{l_S}{2}+l_1\right),\ \left(\frac{l_S}{2}+l_1\right) \leqslant x \leqslant \left(\frac{l_S}{2}+l_1+l_G\right) \\ 1 & -\frac{l_S}{2} \leqslant x \leqslant \frac{l_S}{2} \\ 0 & \text{other} \end{cases} \tag{1}$$

where l_S, l_1, and l_G denote the width of the signal line, the distance between the signal and ground lines, and the width of the ground line, respectively. The $j(x)$ in wave number space can be expressed by Fourier transform as follows [55];

$$j(k) = l_S \mathrm{sinc}\left(\frac{kl_S}{2}\right) - 2l_G \cos\left(k\frac{l_1+l_G+2l_1}{2}\right) \mathrm{sinc}\left(\frac{kl_G}{2}\right). \tag{2}$$

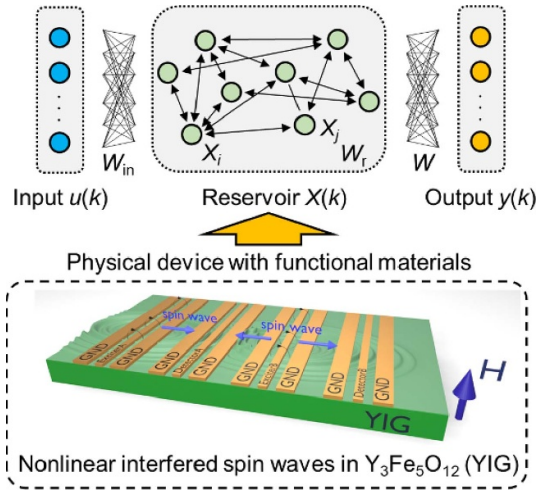

Figure 1. A schematic illustration of reservoir computing utilizing nonlinear interfered spin waves in $Y_3Fe_5O_{12}$ (YIG).

Exciter A and Detector A were connected to a vector network analyzer, and the transmission signal (S_{21} parameter) from Exciter A and Detector A was measured to reveal the actual wave number of spin waves. The spectrum at a magnetic field of 0 mT was subtracted from the spectra obtained at a magnetic field of 100–400 mT to de-embed the transmitted spin wave. The spin wave frequency variation at various H is described as follows [55];

$$f = \gamma \sqrt{(H - H_a)\left\{(H - H_a) + M\left(1 - \frac{1 - e^{-k_w d}}{k_w d}\right)\right\}} \tag{3}$$

where f, γ, H_a, M, k_w, and d represent spin wave frequency, gyromagnetic ratio, magnetic anisotropy field of the YIG, saturation magnetization of the YIG, wave number of spin wave, and YIG thickness, respectively. Here, γ and M were fixed at 2.8 MHz Oe^{-1} [53] and 1984 Gauss [46]. Note that the d used in the calculation is thinner than its thickness. The assumption is that a spin wave propagates at a region that does not correspond to the whole YIG but near the surface at a depth of several micrometers.

2.4. Nonlinear time-series data processing task

The subject reservoir computing system was trained and tested with a random waveform to predict the output from a second-order nonlinear dynamic system and a second-order nonlinear autoregressive moving average (NARMA2) system. These systems are described as follows [56],

$$d(k) = 0.4d(k-1) + 0.4d(k-1)\,d(k-2) + 0.6u^3(k) + 0.1. \tag{4}$$

and

$$d(k+1) = 0.4d(k) + 0.4d(k)\,d(k-1) + 0.6u^3(k) + 0.1. \tag{5}$$

Here, $d(k)$ and $u(k)$ are the output values from the system at k, and the input values at k, respectively. To input to a reservoir computing system, the original random waveform $u(k)$, which ranges from 0 to 0.5, was converted to stepped waveforms. The waveform was separated into training phases with k of 3500 and test phases with k of 500 after the first k of 1000 was discarded. Stepped waveforms were input to the physical reservoir through Exciter A and Exciter B. In the training phase, the weight parameters $\boldsymbol{W}$, shown in figure 1(a), connecting the reservoir part and the readout layer, were learned to minimize the error between the $d(k)$ of equations (4) and (5), and the reservoir output $y(k)$ is described as follows [30, 31, 36, 46]:

$$y(k) = \sum_{i=1}^{n} W_i X_i(k) + b. \tag{6}$$

Here, $X_i(k)$, W_i, n, and b are an i-th node state at k, a weight coefficient connecting $X_i(k)$ and the readout layer, the total number of nodes, and a bias term of 0.1, respectively. W_i was optimized by ridge regression as training for the system to correspond to $d(k)$. On the nonlinear time-series data processing tasks, 50 virtual nodes per detector were from each induced voltage. Thus, 100 reservoir states ('with multi-detection') could

be obtained (i.e. $n = 100$). The inputs were applied sequentially. In order to process this task accurately, using the physical reservoir satisfying nonlinearity, short-term memory, and high dimensionality required for the reservoir is necessary. The NARMA task described in equation (4) represents the required properties (i.e. nonlinearity, short-term memory, and high dimensionality). Because of these system features, predicting the output of the NARMA system is a benchmark task widely used in physical reservoirs, and in this study, which aims to improve speed, it is also an indicator of how long it takes to perform the same task. The relationship between the physical reservoir and time-series data, including short-term memory and nonlinearity, is described in S1 of the supporting information.

2.5. Evaluation of processing performance of the physical reservoir computing

In the time series data analysis tasks, the readout network of the nonlinear interfered spin wave multi-detection reservoir was trained by ridge regression [30, 31, 36, 37, 46]. The reservoir output $y(k)$ shown in equation (6) is transformed to;

$$y(k) = \boldsymbol{W} \cdot \boldsymbol{X}(k). \tag{7}$$

Here, $\boldsymbol{W} = (w_0, w_1, w_i, \ldots, w_n)$ and $\boldsymbol{X}(k) = (X_0(k), X_1(k), X_i(k), \ldots, X_n(k))^{\mathrm{T}}$ are the weight vector and the reservoir state vector with a reservoir size (i.e., the number of nodes) of n, respectively [4]. Note that $w_0 = b$ and $X_0(k) = 1$ to introduce the bias b shown in equation (6). The cost function $J(\boldsymbol{W})$ in the ridge regression is defined as follows;

$$J(W) = \frac{1}{2}\sum_{k=1}^{T}\left(d(k) - y(k)\right)^2 + \frac{\beta}{2}\sum_{i=0}^{N} W_i^2, \tag{8}$$

where T, β and $d(k)$ are the data length in the training phase, the ridge parameter, and the target output generated by equation (4) or equation (5), respectively. $T = 3500$ and $\beta = 0$ were fixed for all the tasks demonstrated in this study. The weight matrix $\widehat{\boldsymbol{W}}$, which minimizes the $J(\boldsymbol{W})$, is written as follows;

$$\widehat{\boldsymbol{W}} = \boldsymbol{Y}\boldsymbol{X}^T\left(\boldsymbol{X}\boldsymbol{X}^T + \lambda \boldsymbol{I}\right)^{-1}. \tag{9}$$

Here, $\boldsymbol{Y} = (d(1), d(2), \ldots, d(T))$, $\boldsymbol{X}(k) = (X(1), X(2), \ldots, X(T))$, and $\boldsymbol{I}$ ($\subseteq \mathbb{R}^{(N+1)\times(N+1)}$) are the target output vector, the reservoir state matrix and the identify matrix, respectively. Here, T is the length of the training phase ($T = 3500$) or test phase ($T = 500$).

After optimizing the $\boldsymbol{W}$, the computational performance of the physical reservoir was evaluated by calculating 'NMSE' for the second-order nonlinear dynamics equation task and '$\mathrm{NMSE}_{\mathrm{var.}}$' for the NARMA2 task to compare its performance with that of other physical reservoirs as following equations [7, 10, 12, 13, 28, 30, 31, 36, 37, 46],

$$\mathrm{NMSE} = \frac{\sum_{k=1}^{T}\left(d(k) - y(k)\right)^2}{\sum_{k=1}^{T}\left(d(k)\right)^2} \tag{10}$$

and

$$\mathrm{NMSE}_{\mathrm{var.}} = \frac{\sum_{k=1}^{T}\left(d(k) - y(k)\right)^2}{\sum_{k=1}^{T}\left(d(k) - d_{ave.}\right)^2}. \tag{11}$$

Here, d_{ave} is the time average of $d(k)$. T is 3500 in the training and 500 in the testing phases.

Operating times of various physical reservoirs were calculated as follows: The number of steps required for training and testing by the physical reservoir in the NARMA task was multiplied by the input time per step (i.e., duration). One waveform consists of 5000 total steps (= discarded 500 steps/training phase of 3500 steps)/discarded 500 steps/testing phase of 500 steps) and a 4 μs interval, where one step corresponds to the total transition time and duration of the input voltage. Since this process is repeated 500 times due to accumulation, all the time required was defined as operating time as follows,

$$\text{Operating time} = (5000\ \text{step} \times \text{duration} + 4\mu s) \times 500. \tag{12}$$

In order to compare the operating time for different physical reservoirs, we calculated it in the same way as above, using the information found in the literature (total number of steps, which are various lengths in the range 500–10 000 depending on studies, and input time per discrete time) [5, 7, 9, 11, 23, 25–27, 30–32, 36, 38, 46, 57].

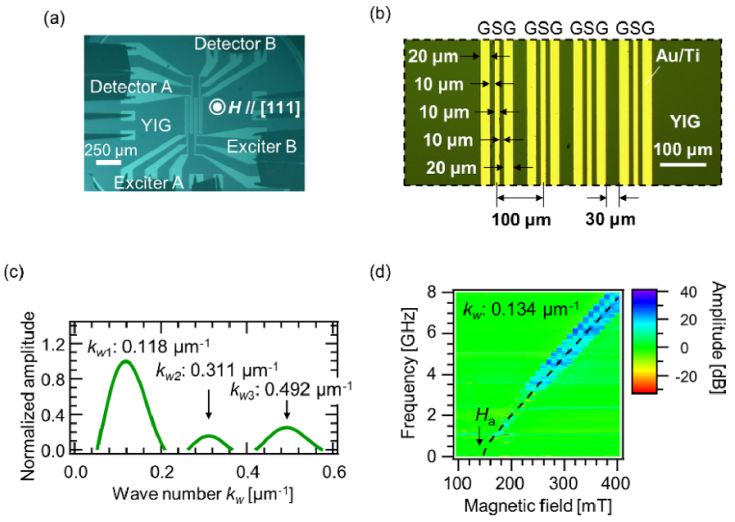

Figure 2. (a) YIG single crystal with deposited coplanar waveguides (CPWs) and its measurement configuration. Magnetic field H is applied perpendicular to the YIG surface. (b) A cropped image of CPWs and their dimensions. G and S represent ground and signal lines. (c) Wave number distribution of electric current density. (d) Magnetic field dependence of spin wave magnetic field.resonance frequency. A dashed line represents a fitting result. H_a denotes an anisotropic.

3. Results

3.1. Physical reservoir computing with nonlinear interfered spin wave and characteristics of the physical device

Figure 1 shows a schematic illustration of a reservoir computing network with a physical device (i.e., physical reservoir computing) in case of utilizing nonlinear interfered spin waves in magnetic material. A reservoir computing network generally has three input, reservoir, and output layers. In particular, the reservoir layer must satisfy critical requirements: nonlinearity, the ability to map input time series data $u(k)$ in high dimensional space, and short-term memory. Thus, such reservoir layer plays a role of nonlinear function mapping $u(k)$ to i-th node state $X_i(k)$ based on its past state $X_i(k-1)$ as follows [4],

$$X_i(k) = f[W_{\text{in}} u(k),\ W_r X_i(k-1)]. \tag{13}$$

Here, W_{in} and W_r denote the weight connecting $u(k)$ to X_i and the weight connecting X_i to j-th node X_j $(i \neq j)$ in the reservoir layer, respectively, and f represents the nonlinear activation function. Increasing the number of i leads to improvement of the ability to map $u(k)$ in high dimensional space. Physical reservoir computing is an innovative scheme that replaces the reservoir layer with a physical device satisfying the above three requirements to implement 'edge computing'. Here, a physical device with nonlinear interfered spin wave multi-detection is realized by utilizing magnetic material and some antennas and is a promising method to realize edge computing with low electrical power consumption.

Figure 2(a) shows an optical microscope image of the physical device with a YIG single crystal. Four coplanar antennas were deposited on the YIG to excite and detect spin waves under the H application. A cropped image of antennas is shown in figure 2(b). The details of fabrication and dimensions of the physical device are described in the experimental section. Since the spin wave is excited by the slope of the electrical signal flowing in the antenna [54], wave number k_w of the excited spin wave corresponds to k_w of $j(x)$. The electric current density calculated from equation (2) is shown in figure 2(c), and a prominent peak and two satellite peaks can be seen. k_{w1} is denoted at the prominent peak, with a full-width half maximum (FWHM) of 0.095 μm^{-1} located at 0.118 μm^{-1}. The remaining two peaks, k_{w2} and k_{w3} with FWHM of 0.067 and 0.095 μm^{-1}, are located at 0.311 and 0.492 μm^{-1}, respectively. Spin wave resonance frequency measurement was carried out to investigate the actual kw of the excited spin wave, as shown in figure 2(d). It was revealed that the wave number of the prominent peak is k_w of 0.134 μm^{-1}, which is in good agreement with k_{w1} of 0.118 μm^{-1} calculated from the distribution of the $j(x)$ shown in figure 2(c). Anisotropic magnetic field H_a can be determined from an intersection with the horizontal axis, and H_a was 1464 Oe.

Figure 3(a) shows a schematic illustration of measurement configuration to detect interfered spin waves at the time domain. In Detector A, spin waves excited at Exciter A and Exciter B interfere and are detected. In Detector B, spin waves excited at Exciter A interfere with spin waves excited at Exciter B and are also affected by the residual precision of the preceding spin wave excited at Exciter B. Figure 3(b) shows spin wave signals

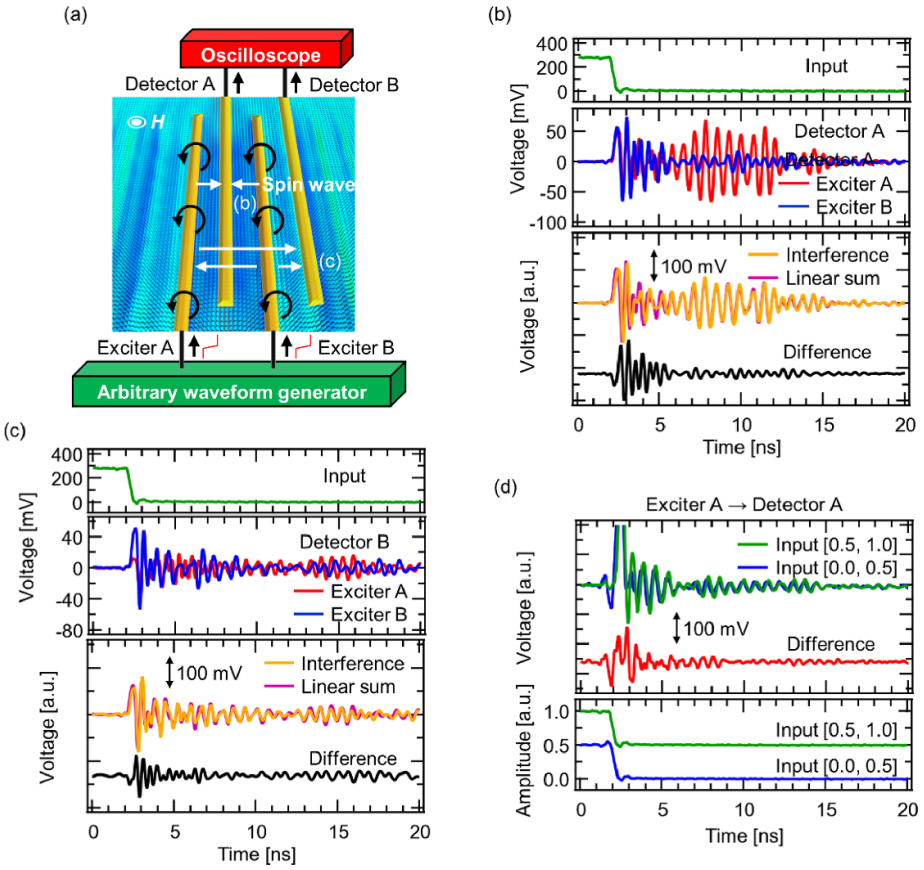

Figure 3. (a) A schematic illustration of measurement configuration to detect interfered spin wave at time domain. Black and white solid arrows represent the magnetic fields induced by electric current and propagating spin waves. Exciter A and Exciter B are CPWs connected to an arbitrary waveform generator, and Detector A and Detector B are CPWs connected to an oscilloscope. (b) (Upper panel) Stepped input voltage. (Middle panel) Spin wave signals, which are excited at Exciter A and Exciter B, detected at Detector A. (Lower panel) Nonlinear interference of spin waves, which are excited at Exciter A and Exciter B, at Detector A. (c) (Upper panel) Stepped input voltage. (Middle panel) Spin wave signals, which are excited at Exciter A and Exciter B, detected at Detector B. (Lower panel) Nonlinear interference of spin waves, which are excited at Exciter A and Exciter B, at Detector B. Difference represents subtracting the linear sum of two waveforms from the Interfered waveform. (d) (Upper panel) Spin wave variation at various base amplitudes of input voltage. (Lower panel) Normalized stepped input. Input [0.5, 1.0] and Input [0.0, 0.5] denote a base level of 0.5 and amplitude of 1.0 and a base level of 0.0 and amplitude of 0.5, respectively.

detected at Detector A and input signals at Exciter A and Exciter B. As shown in the upper panel, a spin wave propagating between Excitor A and Detector A differs from one between Excitor B and Detector A. Thus, a variety of signals can be extracted by the multi-detection. As shown in the lower panel, a finite difference between an interference and a linear summation of spin waves, shown in the upper panel after a time domain of 5 ns, shows that the interfered wave exhibits nonlinearity. This nonlinear interference of spin waves results from magnetic dipole interaction between nonlinearly excited spin waves, as observed in theoretical studies [40, 44, 45]. As shown in figure 3(c), this nonlinear interference was observed at another detector, Detector B. The intensity of the spin wave excited by the step input, defined by the difference between the two values, depends on the source and destination of the step transition, as shown in figure 3(d). Even though input signals have the same amplitude of 0.5, detected signals have different wave packets due to different base amplitudes of 0.0 and 0.5 for input [0.0, 0.5] and input [0.5, 1.0]. This found feature leads that the physical reservoir can distinguish between time series of the same difference (e.g. six different '0.5' expressed by 0.0–0.5, 0.1–0.6, 0.2–0.7, …, and 0.5–1.0) that the input data contains.

3.2. Process flow of physical reservoir computing

Time-series data processing task (e.g., second-order nonlinear equation task and NARMA2 task) is widely performed to evaluate the computational performance of a physical reservoir [7, 10, 12, 13, 28, 30, 31, 36–39, 46]. The process flow for such tasks is shown in figure 4. In solving a second-order nonlinear equation task, $u(k)$ is input to a second-order nonlinear dynamical system. Its $d(k)$ is described as equation (4). The $d(k)$ depends on the input $u(k)$ and the two states $d(k-1)$ and $d(k-2)$ at past steps $k-1$ and $k-2$ in addition to a second-order nonlinear term resulting from the product of $d(k-1)$ and $d(k-2)$. On the other hand, an output $d(k+1)$ is described as equation (5) in the case of the NARMA2 task; the output depends on the $u(k)$

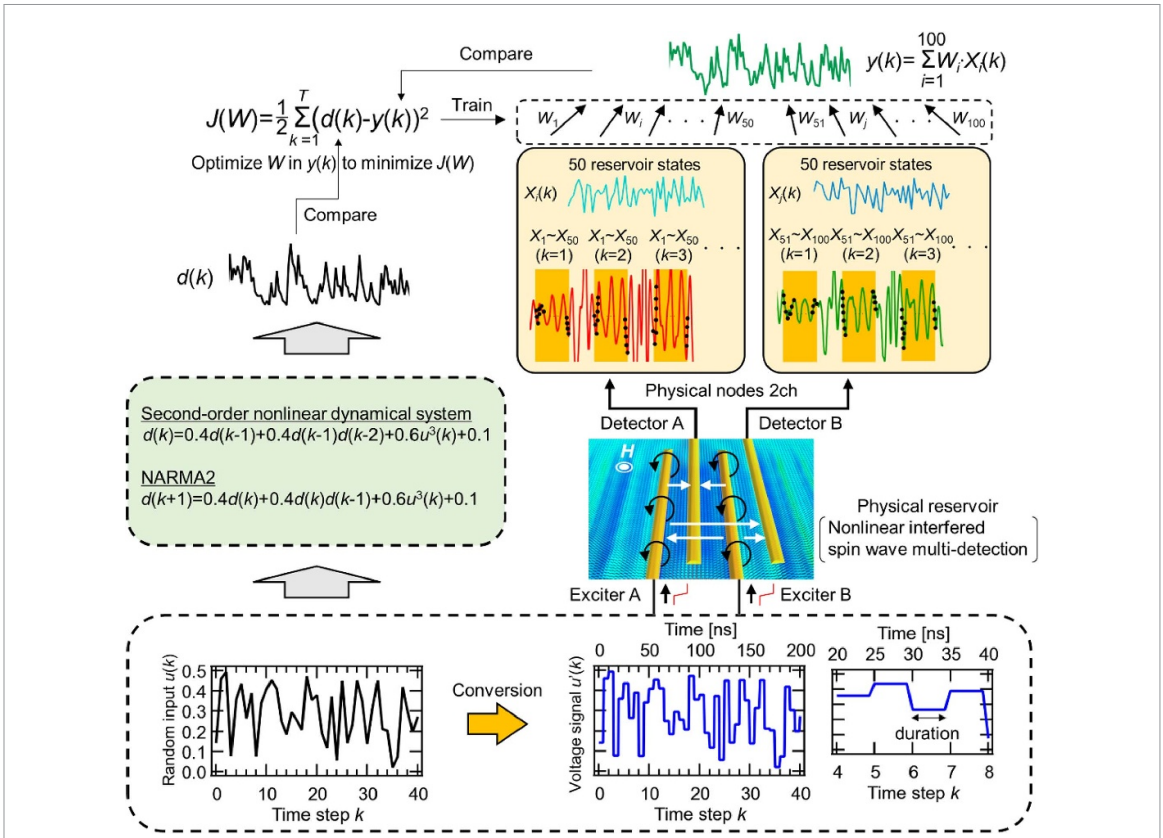

Figure 4. A process flow of time-series data processing task performed by the physical reservoir utilizing interfered spin wave multi-detection. Original random input $u(k)$ is converted to stepped voltage $u'(k)$ with arbitrary duration (e.g. 5 ns). $u(k)$ and $u'(k)$ are input to the theoretical model and physical reservoir. One hundred reservoir states are generated by two physical nodes and 50 virtual nodes taken from nonlinear interfered spin wave multi-detection. Reservoir output $y(k)$ is constructed by linear summation of readout weight Wi and reservoir states $Xi(k)$. Theoretical output $d(k)$ and $y(k)$ are compared to cost function $J(W)$ by optimizing $\boldsymbol{W}$ in $y(k)$.

and the two states $d(k)$ and $d(k-1)$ in addition to a second-order nonlinear term resulting from the product of $d(k)$ and $d(k-1)$. Thus, the physical reservoir is required to satisfy the property shown in equation (12) to solve these tasks precisely. The error of these tasks plays the role of an indicator to evaluate nonlinearity and short-term memory required as the reservoir to process more concrete application tasks, such as spoken-digit recognition task, blood glucose level prediction, abnormal electrocardiogram detection, and sunspot data prediction [4, 9–11, 30, 31, 36–39, 46, 57]. The $u(k)$ is converted to a stepped voltage signal $u'(k)$, and five different $u'(k)$ with five durations of 2, 5, 10, 15, and 20 ns were prepared to explore optimized conditions. Each of these $u'(k)$ is input to the physical reservoir to which perpendicular magnetic fields of 150, 169, 176, 186, 200, and 250 mT are applied. One duration of a stepped signal was equivalent to one discrete time. Then, various spin waves were excited depending on input amplitude. These spin waves propagate toward Detector A and Detector B, interfering with other spin waves, and are converted to voltage signals at two detectors (two physical nodes). The virtual nodes are equally spaced from the whole period within one k. Fifty virtual nodes were taken from the voltage signal, which region does not contain the cross-talk component from the slope of input and which are denoted as black dots in the figure showing the spin wave signals measured at Detector A and Detector B for each k. Then, 100 waveforms were extracted using Detector A and Detector B at k, and a 'reservoir state' was generated. The details of training and testing procedures are described in section 2.4.

3.3. Time-series data processing task

Figure 5(a) shows a comparison with the $d(k)$ of equation (4) and the $y(k)$ in the training phase at the condition under H of 169 mT at a duration of 5 ns. The NMSE defined by equation (10) at this phase is 1.44×10^{-3}. The compared results in the testing phase are shown in figure 5(b). NMSE for this phase exhibits a similar value of 1.39×10^{-3}. Figure 5(c) shows NMSE changes at various durations and H. There is a tendency for NMSE to be lower in weaker H, while NSME in more robust H is higher under all measurement conditions. Although there was no systematic change with different durations, NMSE dropped significantly at durations of 5 and 20 ns, and the lowest NMSE of 1.39×10^{-3} was achieved at H of 169 mT

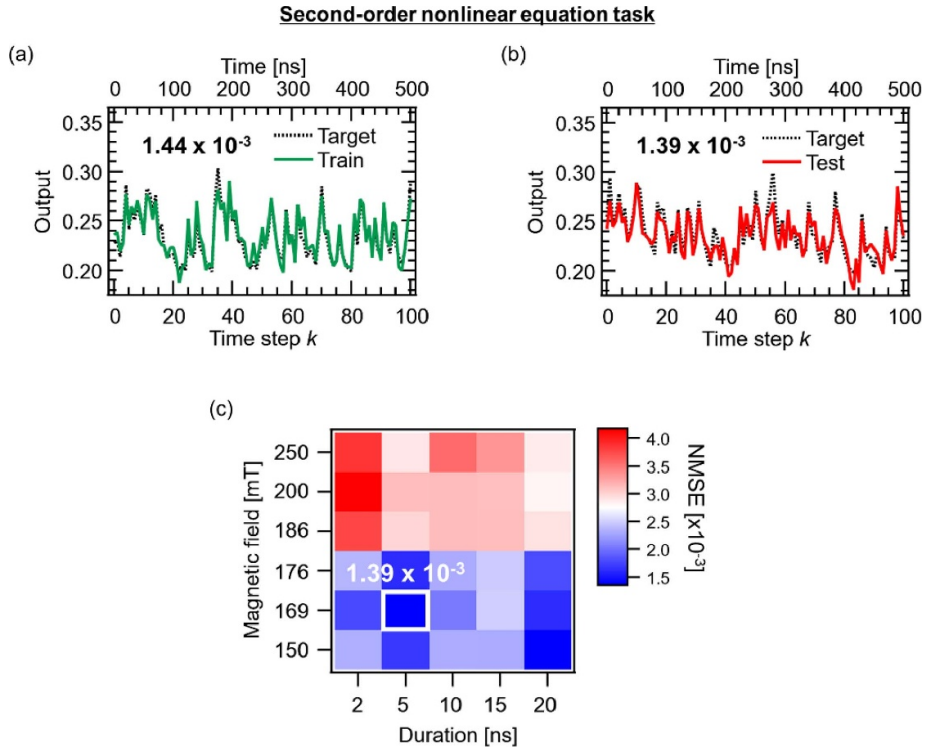

Figure 5. Predicted results at the (a) training phase and (b) test phase of a second-order nonlinear equation task using a duration of 5 ns. The black dotted line, green, and red solid lines represent the target and prediction results at the training and test phases, respectively. (c) NMSE variation of the reservoir computing with interfered spin wave multi-detection for prediction of a second-order nonlinear equation task at various magnetic fields and step durations.

and a duration of 5 ns. This value is lower than or comparable to the values for other physical reservoirs that have been reported, in which the NMSEs of experimental physical reservoirs utilizing 90 metal-oxide memristors and with magnetization vector rotation manipulation were 3.13×10^{-3} and 1.69×10^{-3} [7, 37], and a theoretical physical reservoir utilizing 24 spin torque oscillators was 1.31×10^{-3} [12]. The NARMA is a more difficult task than the former task since, to predict the output of a NARMA model, a physical reservoir is required not only for nonlinearity but also for short-term memory. Here, we introduce NARMA2, which requires short-term memory from the previous two steps, as defined in equation (5).

Figures 6(a) and (b) show comparisons with the $d(k)$ from equation (5) and the $y(k)$ in the training and testing phases at the condition under an H of 169 mT and a duration of 5 ns, for NARMA2. $\mathrm{NMSE_{var}}$ variations at various H and durations are summarized in figure 6(c). The measurement condition dependence of $\mathrm{NMSE_{var}}$ is similar to that of the NMSE. The lowest $\mathrm{NMSE_{var}}$ is 1.71×10^{-1}, which is lower than and comparable to experimental physical reservoirs previously reported [10, 13, 28, 31, 57]. Here, $\mathrm{NMSEs_{var}}$ of surface-functionalized carbon nanotubes [57], the spin torque oscillator (simulated) [13], soft body [28], diode electrical circuit [10], and redox ion-gating reservoir [31] are 0.368, 0.270, 0.192, 0.177, and 0.163, respectively. Thus, it was found that the physical reservoir computing in this study satisfied three critical features as reservoirs and achieved high computational performance comparable to other physical reservoirs [10, 13, 28, 31, 57]. Accumulation number dependence of a signal-to-noise ratio of the detected signal and the computational performance and reproducibility of the time-series data processing are described in S2.1, optimization of length of a training phase and test phase is described in S2.2, and activity of selected nodes in the physical reservoir is described in S3 of the supporting information.

The pulse input corresponding to the input frequency and magnetic field closely relates to equation (3). The frequency of the input pulse is estimated from the rise and fall times of the voltage (280 ps) to be about 1.25 GHz. The magnetic field that satisfies the resonance condition of the spin wave is about 169 mT, as shown in figure 2(d). The spin wave is strongly excited by satisfying the resonance condition, and the computational performance is improved through spin wave interference. In other words, it can be reproduced by applying a pulse input and a magnetic field with a frequency that satisfies the resonance condition expressed in equation (3).

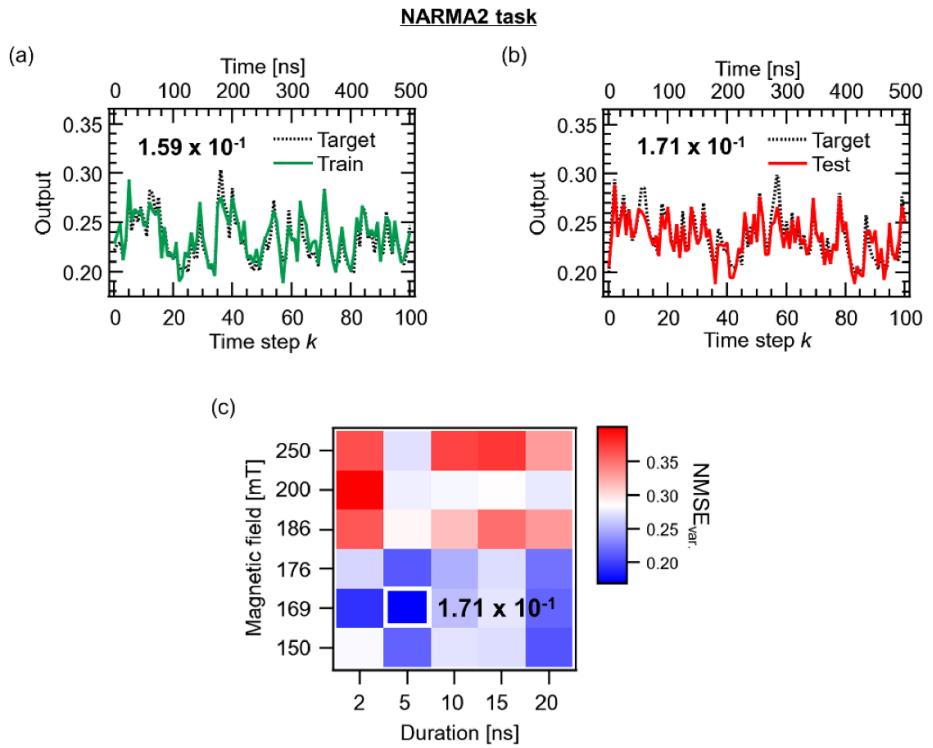

Figure 6. Predicted results at the (a) training phase and (b) test phase of a NARMA2 task using a duration of 5 ns. The black dotted line, green, and red solid lines represent the target and prediction results at the training and test phases, respectively. (c) $NMSE_{var}$ variation of the reservoir computing with interfered spin wave multi-detection for predicting a NARMA2 task at various magnetic fields and step durations.

4. Discussion

4.1. Processing time of physical reservoirs

The advantage of the physical reservoir with stepped input is not only its high performance but also its high-speed processing. Its operating time for a series of input data with 5000-time steps was 13 ms/500 integrations at the duration of 5 ns, corresponding to an operating time of 11.8% faster than the previous study using a pulsed input method with an interval of 5 ns [46]. This dramatic reduction of operating time results from discarding the rising or falling edge and pulse-on time of the pulsed signal due to using a stepped input signal instead of a pulsed one. As shown in figure 7(a), the time for input one pulse signal at k (i.e., t_p) consists of rising and falling edges, pulse-on times, and pulse interval. In contrast, the time for input of one stepped signal at k (i.e., t_s) consists of only the rising edge or falling edge and step duration. Thus, the difference between t_p and t_s is the total time t for the edge and pulse-on, and the absence of t makes the stepped signal shorter (i.e., $t_s = t_{p-}t$).

The operating times of various physical reservoirs are summarized in figure 7(b). The operating time achieved with the stepped input method is the fastest among other physical reservoir computing, which has been carried out in a second-order nonlinear equation task. It corresponds to approximately a discrete time of those physical reservoirs.

Furthermore, the operating time of the physical reservoir utilizing spin wave interference is comparable to some physical reservoirs utilizing optical elements [23, 25–27]. The physical reservoir with spin wave interference is approaching within one order delays, compared with the fastest operating time of 2 ms, achieved with optical element [26], among physical reservoir computing.

The operating time can be further improved by reducing the input duration. This reduction can be realized by adopting magnetic material with higher spin wave frequency. Spin waves with higher frequencies attenuate faster than those with lower frequencies since the duration time of stepped voltage must be adjusted to the decay time, and the duration time must be shortened for fast decay times. Furthermore, since the spin wave is excited by a magnetic field with a specific frequency corresponding to the transition time (i.e. slope) of stepped input voltage, this scheme leads to a reduced slope time per k. When the duration time per k can be set to 500 ps, which is one order faster than this study, and the slope can be shortened, the operating time can be reduced to approximately 1.3 ms, corresponding to 1 order faster than the fastest operating speed in any physical reservoir device.

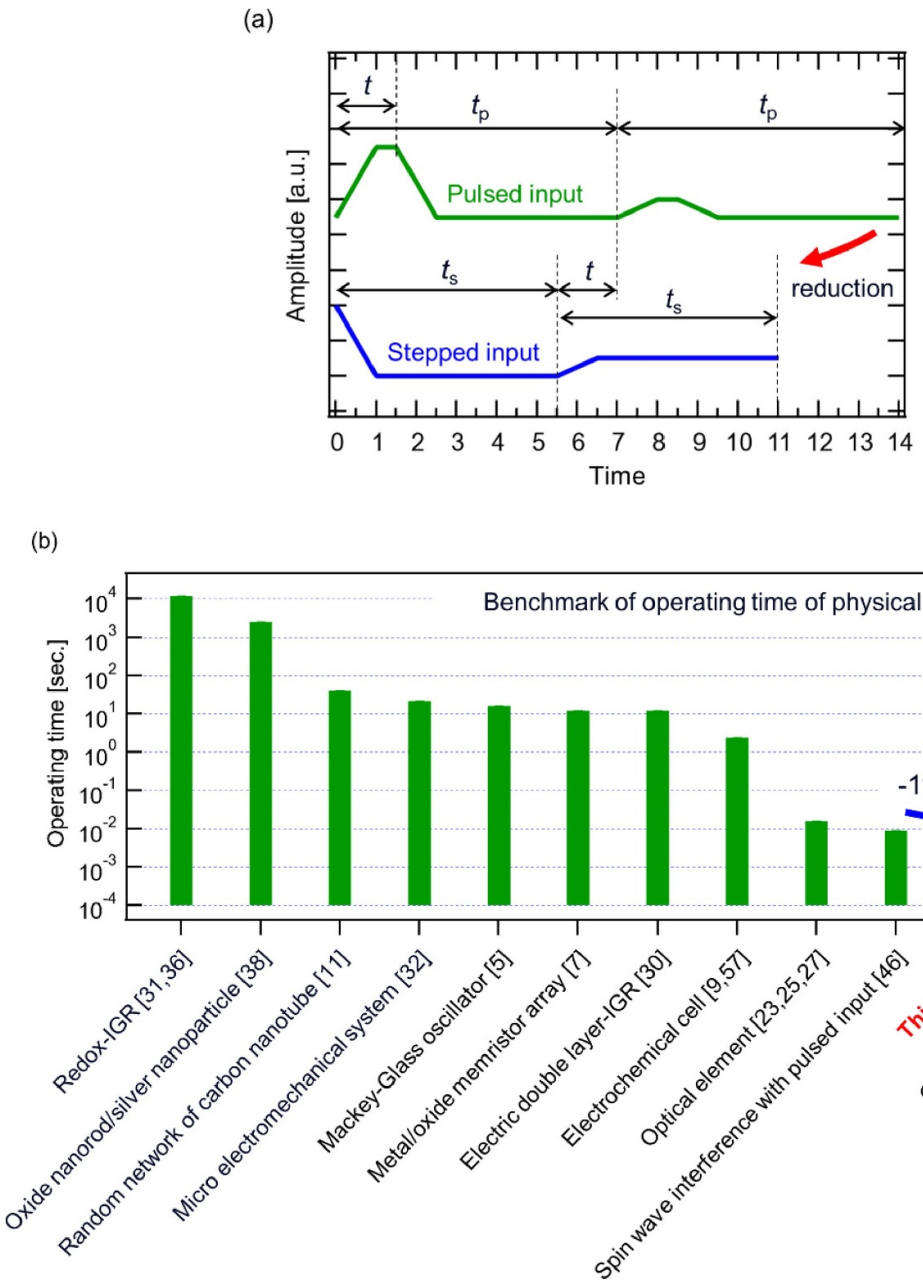

Figure 7. (a) Difference between waveform length of pulsed and stepped input. *tp* and *ts* denote time corresponding to one *k* of pulsed and stepped input, respectively. *t* is the total time of rise and pulse-on. (b) Benchmark of operating time of various physical reservoir devices reported as an experimental demonstration. These operating speeds were calculated from the total time steps used to train and examine the reservoir network, including discarded time steps and time per discrete time [5, 7, 9, 11, 23, 25–27, 30–32, 36, 38, 46, 57].

4.2. Comparing the volume of the physical reservoir

To compare volumes of various physical reservoirs other than the active ring resonator, calculated volumes of various physical reservoirs are summarized in figure 8. The reservoir system using YIG based active ring resonator has volume of $7.8 \times 10^{-3} \sim 4.4 \times 10^{-2}$ cm^3, which are estimated values from dimension (i.e. length $\times$ width $\times$ thickness) of two YIG devices (7.7 mm $\times$ 2.0 mm $\times$ 5.06×10^{-1} mm and 22 mm $\times$ 4.0 mm $\times$ 5.04×10^{-1} mm) [17–19]. Here, the smaller one (i.e. 7.8×10^{-3} cm^3) is the smallest estimation since the length of the YIG is not shown in the reference, and the length of 7.7 mm used in the estimation is the antenna separation, which should be shorter than the YIG length, described in the [17]. The estimated volumes are comparable to or larger than the volume of 9.8×10^{-3} cm^3 (diameter of 5 mm $\times$ 0.5 mm) in the present study. In the spin-wave reservoir using the active ring resonator demonstrated by Watt *et al*, it is necessary to delay the spin wave transmission by lengthening the antenna separation in order to feed back the voltage signal based on the spin wave to the input terminal with a long time difference ranging from approximately 50–215 ns [17–19]. In the studies, antennas were placed on the YIG with a very wide spacing

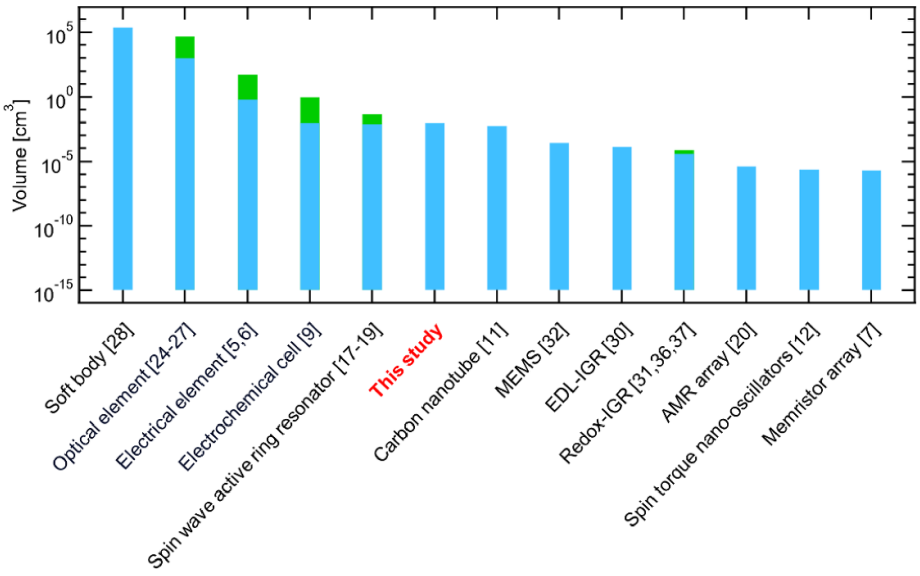

Figure 8. (a) Comparison of volume of physical reservoirs. In addition to this study, physical reservoirs utilizing soft body [28], optical element [24–27], electrical element [5, 6], electrochemical cell [9], spin wave active ring resonator [17–19], carbon nanotube [11], MEMS [32], EDL-IGR [20], redox-IGR [30], AMR array [20], spin torque nano-oscillators [12], and memristor array [7] are shown. Blue and light green bars denote volumes of smaller and larger values.

of 7.7–12 mm to obtain enough delay times [17–19], so the volume of the YIG is large. (The feedback loop in the resonator can be ignored because it does not pose a significant problem for the magnetic volume due to miniaturization techniques.) On the other hand, although we use the same YIG as Watt *et al* in the present study, we reduced the antenna separation of 30 μm by using interfered spin waves and a multi-detection technique. The use of antennas with this short separation allows the device to operate as a smaller reservoir device than the active ring resonator [17–19]. In the future, further miniaturization in thin-film form is expected to reduce the volume through dramatical reducing chip area, and the achieved small volume will be comparable to the volume of the fine physical reservoir with a volume of 10^{-6} cm^{-3} such as spin torque oscillator arrays [12] and memristor arrays [7]. A description of the removal of the electromagnet to simplify the reservoir system is shown in S4 of the supporting information.

4.3. Power consumption of the physical reservoirs

In this study, input information is transferred as a spin wave without Joule loss since a spin wave does not involve a flow of electric charge. Figures 9(a) and (b) show the input voltage signal and the square voltage divided by terminated electrical resistance R of 50 Ω (i.e. V^2/R), respectively, at the region within 1 μs. Here, the total time length per accumulation of input voltage is approximately 26 μs. The electric power [J] is obtained as the time integration of V^2/R. The calculated electrical power is 628 μJ at the condition of inputs using two exciters and 500 times accumulations. The electric power is reduced to 1.26 μJ when the accumulation is no longer necessary.

Echo state networks and liquid state machines, the recurrent neural networks implemented in complementary metal oxide semiconductor (CMOS) circuits, utilize memristor arrays [58, 59]. The electrical power consumption of the echo state network and the liquid state machine are 34.4 and 936 μJ, respectively [58, 59]. Thus, the electric power consumption estimated under the condition without the accumulation is much lower than those networks (i.e. 1.26 μJ (this study) $<$ 34.4 μJ [58] $<$ 936 μJ [59]). The reservoir network and peripheral circuit implemented on the terminal device can be designed based on fine devices such as magnon transistors, operating with a meager energy consumption of 10^{-18} J ($\ll$ CMOS of 10^{-16} J) [50] and readout layer consisting of magnetic tunnel junction array (approximately 50×10^{-15} J) [60]. In this case, the total power consumption of the physical reservoir will be approximately 50×10^{-15} J, which is comparable to the skyrmion-based spintronic physical reservoir (approximately 50×10^{-15} J) [48] in the future.

4.4. Implementation of the output layer

The output of the physical reservoir in this study is an analog circuit. To obtain the reservoir output $y(k)$, the readout requires the following elements: (1) an adder circuit based on a general inverting amplifier circuit for integration, (2) an analog-to-digital converter (ADC), (3) a demultiplexer (DEMUX) to extract the nodes,

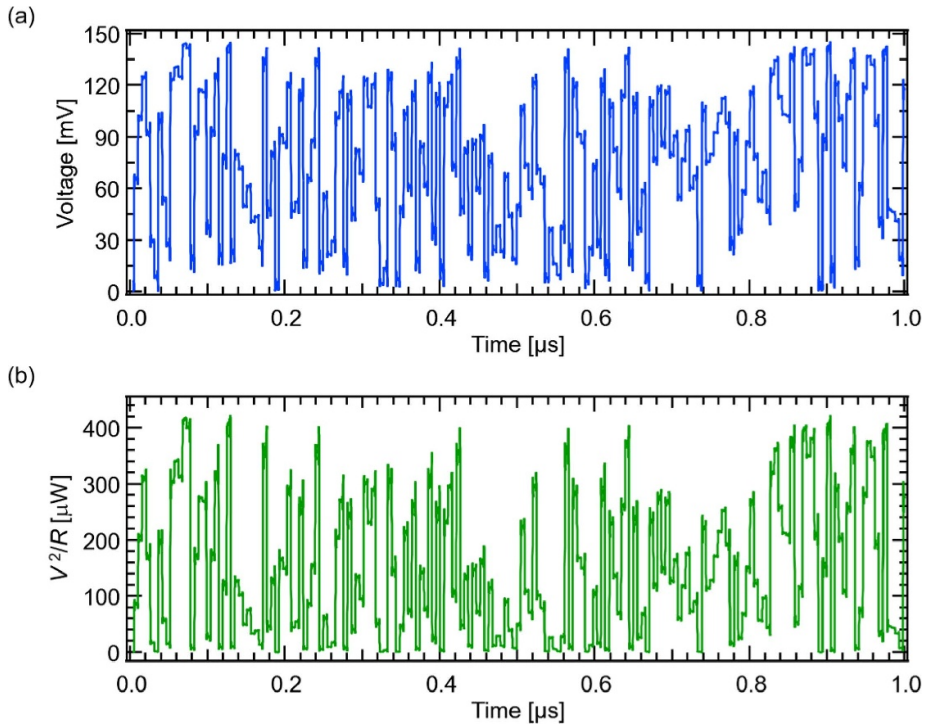

Figure 9. (a) Input voltage signal and (b) the square voltage divided by terminated electrical resistance R of 50 Ω (i.e. V^2/R), respectively, at the region within 1 μs. A total time of input per accumulation is approximately 26 μs.

(4) a memristor crossbar array for readout weights, (5) a multiply-accumulate to compute the sum of products (i.e. $y(k)$) of weights and reservoir states. All elements can be fabricated using conventional lithographic techniques [47]. It has been demonstrated that a memristor crossbar array implemented in a CMOS circuit can represent 2048 electrical resistances and can be used sufficiently as a weight matrix [61]. It is known that an ADC can be omitted by restricting the input to the reservoir and the output of the readout memristor crossbar array to binary [47], but in this study, the ADC is necessary because the task is to take analog random waveforms as input.

We assumed the peripheral circuits required for the physical reservoir in this study and estimated their area, power, and delay. The peripheral circuits of the physical reservoir were based on previous studies of physical reservoirs implemented up to the readout layer [47]. It is assumed that an adder will be used to accumulate the analog voltage signal induced by the spin wave, and a demultiplexer will be used to extract the 100 nodes multiplexed into that voltage signal. The retrieved reservoir states are then weighted in a memristor crossbar array and summed in a MAC circuit to produce a reservoir output. An ADC is inserted between the adder and DEMUX to convert the voltage signal to a digital signal. It is assumed that the target data for training the reservoir output is converted to digital signals by the ADC to adjust the electrical resistance (i.e. output layer weights) of the memristor crossbar array.

The number of nodes and the length of the output vector is represented by N and L. The feature size (S) of the peripheral circuit is assumed to be 65 nm (i.e. $S = 65$ nm) [47]. The area of the NMOS and PMOS transistors are assumed to be $4S^2$ and $8S^2$, respectively [47]. For a 2-input adder, 11 NMOS and 11 PMOS transistors (i.e., 22 in total) are used each, and the area of the adder for 500 inputs corresponding to 500 integrations is $250 \times 11 \times (4S^2 + 8S^2) = 13.94$ μm^2 [58]. An analog-to-digital converter (ADC) consists of 2^n–1 comparators depending on the number of bits n. The area of an n-bit ADC is represented by $(2^n - 1) \times 52S^2$, which is approximately 56–224 μm^2 ($n = 8$–10 bits) [59]. A 4ch DEMUX consists of 14 NMOS and 14 PMOS, and the area of a DEMUX with 100 channels is $14 \times (4S^2 + 8S^2) \times 25 = 17.8$ μm^2. The area of a memristor is $10S^2$ [47], and the area of the memristor crossbar array connected between the N of 100 and the output layer is $10S^2 \times N \times L = 423$ μm^2. Finally, assuming that each multiplication-and-accumulation consists of 3 NMOS [60], its area is $(4S^2 \times 3) \times 100$ nodes $= 5.07$ μm^2.

The power consumption of the memristor is 5.05 fJ, and from 100 nodes and the length of output vectors, the power consumption of the memristor crossbar array is 5.05 fJ $\times$ 100 $\times$ 100 = 50.5 pJ. For other CMOS circuits, the power consumption of the adder is 0.176 fJ [58], the power consumption of the ADC is 151 nJ [59]. Since the power consumption of the physical reservoir is 628 μJ (500 times integration) and

1.26 μJ without integration, the power consumption of the memristor crossbar array and typical peripheral CMOS circuitry is sufficiently small compared to that of the physical reservoir.

Assuming implementation, the delay due to the readout layer is 0.1–35 ns in CMOS circuits [58, 59]. Since the operating time of the physical reservoir is 26 μs $\times$ 500 accumulation, the readout is completed in a very short time compared to the input time of the time series data.

4.5. Reduction of applied magnetic field

The magnetic field ranging from 150 to 250 mT was used to investigate the measurement condition dependence of the computational performance, and it was found that the magnetic field for the highest computational performance was 169 mT. The applied magnetic field must satisfy the resonance condition under which spin waves are strongly excited. For a given input frequency, the magnetic field that excites spin waves is determined by equation (3), and the computational performance becomes high near this magnetic field. In this study, the magnetic field of 169 mT satisfies the resonance condition, and the magnetic field was varied around this field from 150 to 250 mT to verify the magnetic field dependence. The resonance condition is described by anisotropic magnetic field H_a and saturation magnetization M, as shown in equation (3). It thus varies depending on the magnetic material and shape (bulk or thin film) with different magnetic properties. If the use of a large magnetic field will affect high-speed processing, the use of ferromagnetic materials with perpendicular magnetic anisotropy will reduce the external magnetic field, thus preserving the high speed of reservoir computing using spin-wave interference demonstrated in this study.

To reduce the amplitude of the magnetic field, the selection of magnetic material with strong magnetic anisotropy as the physical reservoir is needed. The YIG single crystal used in this study has in-plane spontaneous magnetization, meaning that a large magnetic field is required to align the magnetization with the out-of-plane direction. Here, when any magnetic material with out-of-plane spontaneous magnetization is used, a large magnetic field along the out-of-plane is not required. Thus, the required magnetic field will be successfully reduced. It is known that some magnetic material in the thin film form shows perpendicular magnetic anisotropy [62, 63]. Demonstrating physical reservoir computing, which can operate under or without a small magnetic field application, is a future challenge to improve its practicality.

In conclusion, we demonstrated physical reservoir computing utilizing spin wave interference with a stepped input method. The physical device used in this study consists of a typical ferrimagnetic YIG and multiple CPWs. The time-series data processing task, second-order nonlinear equation task, and NARMA2 prediction task were carried out to evaluate the performance of said physical reservoir. NMSE and $\mathrm{NMSE_{var}}$ of the former and the latter were 1.39×10^{-3} and 1.71×10^{-1}, respectively. These errors are lower than or comparable to other compact physical reservoirs. Operating time at 5 ns step duration was successfully reduced by 11.8%, compared to the physical reservoir utilizing spin wave interference with a pulsed input method at a pulse interval of 5 ns [46]. This physical reservoir achieved the fastest operating time among compact physical reservoirs. A much shorter operating time can be realized by utilizing spin waves with higher frequency, and it can transcend the fastest operating speed of optical circuits and physical devices with huge volumes in the future.

Data availability statement

The data cannot be made publicly available upon publication because no suitable repository exists for hosting data in this field of study. The data that support the findings of this study are available upon reasonable request from the authors.

Acknowledgments

Innovative Science and Technology Initiative for Security Grant Number JPJ004596, ATLA, Japan supported this work. This work was partly supported by the Japan Society for the Promotion of Science (JSPS), KAKENHI Grant number, JP21J21982 (Grant-in-Aid for JSPS Fellows). A part of this work was supported by 'Advanced Research Infrastructure for Materials and Nanotechnology in Japan (ARIM)' of the Ministry of Education, Culture, Sports, Science and Technology (MEXT). Proposal Number JPMXP1223NM5072. Part of this work was supported by the Electron microcopy unit of the National Institute for Materials Science.

ORCID iDs

Wataru Namiki https://orcid.org/0000-0003-4053-7366
Daiki Nishioka https://orcid.org/0000-0002-3369-7700
Takashi Tsuchiya https://orcid.org/0000-0002-6950-6160

References

[1] Jaeger H and Haas H 2004 *Science* **304** 78
[2] Maass W, Natschläger T and Markram H 2002 *Neural Comput.* **14** 2531
[3] Verstraeten D, Schrauwen B, D'Haene M and Stroobandt D 2007 *Neural Netw.* **20** 391
[4] Tanaka G, Yamane T, Heroux J B, Nakane R, Kanazawa N, Takeda S, Numata H, Nakano D and Hirose A 2019 *Neural Netw.* **115** 100
[5] Appeltant L, Soriano M C, van der Sande G, Danckaert J, Massar S, Dambre J, Schrauwen B, Mirasso C R and Fischer I 2011 *Nat. Commun.* **2** 468
[6] Appeltant L, van der Sande G, Danckaert J and Fischer I 2014 *Sci. Rep.* **4** 3629
[7] Du C, Cai F, Zidan M A, Ma W, Lee S H and Lu W D 2017 *Nat. Commun.* **8** 2204
[8] Midya R, Wang A, Asapu S, Zhang X, Rao M, Song W, Zhuo Y, Upadhyay N, Xia Q and Yang J J 2019 *Adv. Intell. Syst.* **1** 1900084
[9] Kan S, Nakajima K, Asai T and Kasaya M A 2022 *Adv. Sci.* **9** 2104076
[10] Kan S, Nakajima K, Asai T, Kasaya M A, Kuwahara Y and Akai-Kasaya M 2021 *Phys. Rev. Appl.* **15** 024030
[11] Kasaya M A, Takeshima Y, Kan S, Nakajima K, Oya T and Asai T 2022 *Neuromorph. Comput. Eng.* **2** 014003
[12] Jiang W, Chen L, Zhou K, Li L, Fu Q, Du Y and Liu R H 2019 *Appl. Phys. Lett.* **115** 192403
[13] Akashi N, Yamaguchi T, Tsunegi S, Taniguchi T, Nishida M, Sakurai R, Wakao Y and Nakajima K 2020 *Phys. Rev. Res.* **2** 043303
[14] Kanao T, Suto H, Mizushima K, Goto H, Tanamoto T and Nagasawa T 2019 *Phys. Rev. Appl.* **12** 024052
[15] Tsunegi S, Taniguchi T, Nakajima K, Miwa S, Yakushiji K, Fukushima A, Yuasa S and Kubota H 2019 *Appl. Phys. Lett.* **114** 164101
[16] Taniguchi T, Ogihara A, Utsumi Y and Tsunegi S 2022 *Sci. Rep.* **12** 10627
[17] Watt S, Kostylev M and Ustinov A B 2021 *J. Appl. Phys.* **129** 044902
[18] Watt S and Kostylev M 2020 *Phys. Rev. Appl.* **13** 034057
[19] Watt S, Kostylev M, Ustinov A B and Kalinikos B A 2021 *Phys. Rev. Appl.* **15** 064060
[20] Vidamour I T *et al* 2023 *Commun. Phys.* **6** 230
[21] Nakajima M, Tanaka K and Hashimoto T 2021 *Commun. Phys.* **4** 20
[22] Sunada S and Uchida A 2019 *Sci. Rep.* **9** 19078
[23] Okumura T, Tai M and Ando M 2019 *Nonlinear Theory Appl.* **10** 236
[24] Paquot Y, Duport F, Smerieri A, Dambre J, Schrauwen B, Haelterman M and Massar S 2012 *Sci. Rep.* **2** 287
[25] Duport F, Smerieri A, Akrout A, Haelterman M and Massar S 2016 *Sci. Rep.* **6** 22381
[26] Vinckier Q, Duport F, Smerieri A, Vandoorne K, Bienstman P, Haelterman M and Massar S 2015 *Optica* **2** 438
[27] Hermans M, Antonik P, Haelterman M and Massar S 2016 *Phys. Rev. Lett.* **117** 128301
[28] Nakajima K, Hauser H, Li T and Pfeifer R 2015 *Sci. Rep.* **5** 10487
[29] Koh S G, Shima H, Naitoh Y, Akinaga H and Kinoshita K 2022 *Sci. Rep.* **12** 6958
[30] Nishioka D, Tsuchiya T, Namiki W, Takayanagi M, Imura M, Koide Y, Higuchi T and Terabe K 2022 *Sci. Adv.* **8** eade1156
[31] Wada T, Nishioka D, Namiki W, Tsuchiya T, Higuchi T and Terabe K 2022 *Adv. Intell. Syst.* **5** 2300123
[32] Brazani B, Dion G, Morissette J-F, Beaudoin L and Sylvestre J 2020 *J. Microelectromech. Syst.* **29** 338
[33] Gartside J C, Stenning G D, Vanstone A, Holder H H, Arroo D M, Dion T, Caravelli F, Kurebayashi H and Branford W R 2022 *Nat. Nanotechnol.* **17** 460
[34] Maraj J J, Haughn K P T, Inman D J and Sarles S A 2023 *Adv. Intell. Syst.* **5** 2300049
[35] Nakajima M, Inoue K, Tanaka K, Kuniyoshi Y, Hashimoto T and Nakajima K 2022 *Nat. Commun.* **13** 7847
[36] Shibata K, Nishioka D, Namiki W, Tsuchiya T, Higuchi T and Terabe K 2023 *Sci. Rep.* **13** 21060
[37] Namiki W, Nishioka D, Tsuchiya T, Higuchi T and Terabe K 2024 *Nano Lett.* **24** 4383–92
[38] Nishioka D, Shingaya Y, Tsuchiya T, Higuchi T and Terabe K 2023 *Sci. Adv.* **10** adk6438
[39] Nishioka D, Tsuchiya T, Imura M, Koide Y, Higuchi T and Terabe K 2023 (arXiv: 2309.03028)
[40] Nakane R, Tanaka G and Hirose A 2018 *IEEE Access* **6** 4462
[41] Nakane R, Hirose A and Tanaka G 2021 *Phys. Rev. Res.* **3** 033243
[42] Ichimura T, Nakane R, Tanaka G and Hirose A 2021 *IEEE Access* **9** 72637
[43] Nakane R, Hirose A and Tanaka G 2023 *Phys. Rev. Appl.* **19** 034047
[44] Papp A, Csaba G and Porod W 2021 *Appl. Phys. Lett.* **119** 112403
[45] Papp A, Porod W and Csaba G 2021 *Nat. Commun.* **12** 6422
[46] Namiki W, Nishioka D, Yamaguchi Y, Tsuchiya T, Higuchi T and Terabe K 2023 *Adv. Intell. Syst.* **5** 2300238
[47] Edwards A J *et al* 2023 *Commun. Phys.* **6** 215
[48] Rajib M M, Misba W A, Chowdhury M F F, Alam M S and Atulasimha J 2022 *Neuro. Comput. Eng.* **2** 4
[49] Prychynenko D, Sitte M, Litzius K, Kruger B, Bourianoff G, Klaui M, Sinova J and Everschor-Sitte K 2018 *Phys. Rev. Appl.* **9** 014034
[50] Chumak A V, Serga A A and Hillebrands B 2014 *Nat. Commun.* **5** 4700
[51] Jamali M, Kwon J H, Seo S-M, Lee K-J and Yang H 2013 *Sci. Rep.* **3** 3160
[52] Klingler S, Pirro P, Brächer T, Leven B, Hillebrands B and Chumak A V 2015 *Appl. Phys. Lett.* **106** 212406
[53] Goto T, Yoshimoto T, Iwamoto B, Shimada K, Ross C A, Sekiguchi K, Graovsky A B, Nakamura Y, Uchida H and Inoue M 2019 *Sci. Rep.* **9** 16472
[54] Wu M, Kalinikos B A, Krivosik P and Patton C E 2006 *J. Appl. Phys.* **99** 013901
[55] Vlaminck V and Bailleul M 2010 *Phys. Rev.* B **81** 014425
[56] F A A and Parlos A G 2000 *IEEE Trans. Neural Netw.* **11** 697
[57] Shingu T, Uchiyama H, Watanabe T and Ohno Y 2023 *Carbon* **214** 118344
[58] Mewada M, Zaveri M, Gandhi R and Thakker R 2020 *Proc. Commun. Sci.* 171 999
[59] Hussain S, Kumar R and Trivedi G 2021 *IOP Conf. Ser.: Mater. Sci. Eng.* **1020** 012022
[60] Wang Y *et al* 2021 *Nat. Commun.* **12** 3347
[61] Rao M *et al* 2023 *Nature* **615** 823
[62] Kwon J H, Yoon J, Derorani P, Lee J M, Shinha J, Lee K-J, Hayashi M and Yang H 2016 *Adv. Sci.* **2** e1501892
[63] Sheng L *et al* 2020 *Appl. Phys. Lett.* 117 232407